

RESEARCH ARTICLE

Static analysis of functionally graded piezoelectric plates via an isogeometric layerwise finite element

Kazım Ahmet Haşim^{1*}

Adana Alparslan Türkeş Science and Technology University, Department of Civil Engineering, Adana, Türkiye

Article History

Received 18 November 2024 Accepted 18 December 2024

Keywords

Piezoelectric
Functionally graded
Isogeometric
Layerwise
Finite element

Abstract

In this study, an isogeometric finite element originally developed for piezolaminated plates has been extended and named FGL-IGA to perform the static analysis of thick and thin functionally graded piezoelectric plates. Unlike most of the isogeometric finite element models in literature that neglect thickness stretching when analyzing through-the-thickness functionally graded plates, FGL-IGA integrates Reddy's layerwise theory into the electromechanically coupled constitutive and equilibrium equations, enabling precise displacement and stress results relying on the displacement-based virtual work principle. Additionally, unlike standard finite elements, the utilization of high-order continuous NURBS functions for discretizing geometry and kinematic variables allows both direct and exact retrieval of geometry from CAD software, as well as faster convergence of results. The accuracy and reliability of FGL-IGA have been tested and validated for two cases with exact solutions from literature, considering various span-to-thickness ratios and electromechanical loading scenarios.

1. Introduction

In the late 1980s, a group of Japanese scientists introduced the concept of functionally graded materials (FGM), which refers to a smooth and continuous variation of mechanical properties from one surface to another [1, 2]. The unique idea of FGMs emerged from the requirement of heat-resistant ceramic materials to be used as thermal barriers on surfaces with high temperatures, while utilizing tough metals with high thermal conductivity on the opposite surface, resulting in a gradual compositional variation from ceramic to metal. Evaluation of the mechanical properties in FG structures, two different approaches have been used in literature, that are the theory of mixtures or Mori-Tanaka scheme [3]. Due to their high-performance and multi-functional roles, FGMs gained considerable attention by the future high-speed spacecraft and power generation industries [4]. Many investigations have been carried out to assess the behaviour of functionally graded plates and shells. Reddy [5] has proposed a Navier's solution for the analysis of through-the-thickness FG plates accounting for the Von-Karman type geometric nonlinearity. A closed form solution by Cheng and Batra [6] has been developed for the analysis of linear thermoelastic, functionally graded elliptic plates. Carrera et al. [7] considered the theories employing a constant transverse displacement in FG structures as a

^{*} Corresponding author (kahasim@atu.edu.tr)

contradiction since the material properties change significantly through-the-thickness. To investigate the effect of thickness stretching, Carrera's Unified Formulation (CUF) [8] has been extended to FG plates in [9–11].

The abilities of piezoelectric materials to generate electrical voltage under mechanical stress (direct effect) and deformations in response to an applied electrical field (converse effect) allow their use as actuators and sensors in smart structures with self-controlling capabilities [12]. Until recently, monolithic piezoelectric materials such as Piezoceramics (like PZT) and Piezopolymers (like PVDF) played a major role in active damping in smart structures. Higher electromechanical coupling coefficient compared to piezoelectric polymers makes the PZTs more efficient. Nonetheless, there are still notable disadvantages associated with strip-form piezoceramic sheets that are bonded using an adhesive, such as epoxy resin. PZTs are brittle, unflexible and when subjected to low temperatures, interfacial stress concentrations between two piezoelectric ceramic sheets can trigger the crack initiation and propagation, resulting in layer detachments, while at high temperatures, creep may take place [13]. To attain high piezoelectric effect from PZTs and ductility from PVDFs, today's production technology has fulfilled these requirements by producing a new kind of material, named as functionally graded piezoelectric material (FGPM) in which the piezoelectric and dielectric material coefficients vary continuously and gradually along the thickness. Piezoelectric structures can be entirely made by FGPMs or utilizing an FG core layer with an outer skin, made by piezoelectric fiber reinforced composites (PFRC). The rods of piezoelectric materials in PFRCs are generally oriented longitudinally embedded in a polymer matrix and the electrical field is applied across the thickness of the composite, that is, in a direction transverse to the fiber alignment. Mallik and Ray [14] have proven that PFRCs are superior to monolithic ones by determining the effective coefficient of PFRCs. In recent years, numerous studies have been published to examine the behaviour of functionally graded piezoelectric materials. For example, Ray and Sachade [15] have developed a finite element model (FEM) for the static analysis of functionally graded plates incorporating a layer of PFRC material and compared the FEM results with the exact solutions of [16]. Based on 3D electroelasticity theory, Zhong and Shang [17] have presented an exact solution for a FGPM, simply supported plate. Zenkour and Alghanmi [18] have investigated the static response of a sandwich plate composed of FG core and piezoelectric faces under hygro-thermo-electromechanical sinusoidal loadings by employing a two-variable shear deformation plate theory. Also, Rouzegar and Abbasi [19] have conducted a FE formulation utilizing a four-variable refined plate theory to predict the displacement and stress results of the FG plate integrated with a PFRC actuator under electrical and mechanical loadings. Shiyekar and Kant [20] have derived an analytical solution for the bending analysis of laminates with PFRC actuators using a higher order shear and normal deformation theory. Recently, Chanda and Sahoo [21] have studied the flexural behaviour of smart FG plate with PFRC actuator at the top/bottom by employing the inverse hyperbolic shear deformation theory. Dung et al. [22] have examined the static bending and dynamic response analyses of piezoelectric bidirectional FG plates, utilizing a combination of Reddy's third order shear deformation theory and FEM.

In recent years, Hughes et al. [23, 24] introduced a method known as isogeometric analysis (IGA). This approach utilizes Non-Uniform Rational B-Splines (NURBS) basis functions for both kinematic variable approximation and geometry definition, paralleling their use in Computer Aided Design (CAD) for exact geometric representation. Thus, geometric data from CAD could be maintained at the coarsest level of discretization and employed directly for numerical simulation purposes. The notable attributes of IGA, including higher-order continuity, elimination of the meshing difficulty, and the maintanance of geometric accuracy throughout the analysis, make it a more advanced option compared to traditional FEM. An overview along with the computational implementation of IGA was provided in [25]. IGA has been effectively applied to linear analyses of FGM structures, particularly in FG plates and shells [26, 27]. Besides, Liu et al. [28] proposed a NURBS based IGA on the basis of first order shear deformation theory for analysing the static

and dynamic responses of FG plates with surface-bonded piezoelectric actuators and sensors. Chen et al. [29] also utilized IGA to investigate the vibration and transient responses of FGPM curved beams. Further, Shi [30] has developed an isogeometric finite element for the static bending, free vibration and buckling behaviours of FG carbon nanotube-reinforced composite plates. Nguyen-Thoi et al. [31] have presented a numerical approach that combines electromechanical coupling IGA with a piecewise linear zig-zag function to analyze multilayer porous FG graphene platelets-reinforced composite plates.

The literature indicates that the deformation response of functionally graded plates with piezoelectric actuators has been investigated using equivalent single layer (ESL) theories, either First-Order Shear Deformation Theory (FSDT) or Higher-Order Shear Deformation Theories (HSDTs). However, it is noted that the results from FSDT are often unreliable for thick multilayered composite or functionally graded plate structures. Besides, HSDTs incorporate higher-order terms, which account for additional membrane and bending deformation modes necessary for accurately modelling non-homogeneous multilayered plates. Nonetheless, these higher-order terms can sometimes be difficult to realize physically. Also, Qian et al. [32] highlighted that most of the ESL theories in literature disregard transverse normal deformations and generally assume that the FG plate is under a plane stress condition. While these assumptions are appropriate for thin plates, they may lead to inaccurate results for thicker ones with a length/thickness ratio of 5 or lower. When the main emphasis of the analysis is on determining accurate prediction of through-the-thickness stress and electrical displacement values of thick FGP plates, Layerwise Theories (LWTs) based FE models provide a more realistic kinematics assumption with separate displacement and electrical potential field expansions for each material layer through the laminate thickness [33–36].

To the best of the authors' knowledge, the isogeometric studies conducted in literature on FGP plates are based on the ESL theories that disregard thickness stretching. It is evident that these studies, even when utilizing high-order continuous NURBS functions, will not yield accurate and reliable stress and displacement results in thick FG plates when compared to LW theory, which considers deformation in the thickness direction. To fulfil this gap, the IGA-based LW finite element developed for the static analysis of piezolaminated plates, has been extended in this study to perform the static analysis of both thin and thick FG plates with integrated piezoelectric layers [35]. To evaluate the current Functionally Graded Layerwise IsoGeometric (FGL-IGA) methodology, several analyses with different span/thickness ratios and electromechanical loadings scenarios have been performed utilizing an in-house Mathematica code that imports the exact geometric NURBS data from the commercial Rhinoceros CAD software. The accuracy and reliability of the FGL-IGA have been verified by comparing the results with the analytical solutions in literature [16, 17]. The outline of the paper is as follows: Section 2.1 addresses the governing piezoelectric equations, providing a brief explanation of the variation in material properties, constitutive equations, and the weak formulation related to FGPMs. Sections 2.2 and 2.3 respectively give a concise overview of Bsplines and NURBS basis functions, as well as the isogeometric layerwise kinematics for FGP plates. In Section 3, an in-depth analysis is performed to demonstrate the effects of electromechanical coupling, the functionally graded index, and the span/thickness ratio on the static bending response. The paper is finalized with concluding remarks included in Section 4.

2. Mathematical formulation

Consider a simply supported, rectangular plate made of FG material, as shown in Fig. 1. The top surface of the plate is integrated with a layer of PFRC material, which serves as the distributed actuator for the FG plate. The dimensions of the plate length, width, and thickness are designated as a, b, and h, respectively, while the thickness of the PFRC layer is represented by h_p . The bottom surface of the FG substrate plate, $x_3 = 0$ is treated as the reference plane, and the origin of the Cartesian coordinate system, $\{x_i\}$ (i = 1,2,3) is

positioned at one corner of the bottom surface. The coordinates $x_1 = 0$, a and $x_2 = 0$, b correspond to the edges of the FG substrate plate.

The displacements, $\mathbf{u} = \{u_1 \ u_2 \ u_3\}^T$ and the electrical potential, ϕ_p illustrated in Fig. 1, are both regarded as primary variables. In accordance with the layerwise description, each physical layer (either in FG substrate or actuator) can be separated into computational k sublayers. The superscript, k stands for the kth layer specifics.

2.1. Electro-mechanical basic equations

Under the assumptions of linear piezo-elastic material behavior and small strain-small displacements, the electromechanical coupling (direct piezoelectric effect) between the elastic and electric field for a single piezoelectric kth layer can be expressed as follows:

$$\boldsymbol{\sigma}^{(k)} = \bar{\boldsymbol{Q}}^{(k)} \boldsymbol{\varepsilon}^{(k)} - \bar{\boldsymbol{e}}^{(k)} \boldsymbol{E}^{(k)}$$
 (1a)

$$\mathbf{D}^{(k)} = \bar{\mathbf{e}}^{(k)} \mathbf{\varepsilon}^{(k)} + \bar{\mathbf{\Lambda}}^{(k)} \mathbf{E}^{(k)}$$
(1b)

$$\boldsymbol{\sigma}^{(k)} = \left\{ \sigma_1^{(k)} \quad \sigma_2^{(k)} \quad \sigma_3^{(k)} \quad \tau_{13}^{(k)} \quad \tau_{23}^{(k)} \quad \tau_{12}^{(k)} \right\}^T \tag{2a}$$

$$\boldsymbol{\varepsilon}^{(k)} = \left\{ \boldsymbol{\varepsilon}_{1}^{(k)} \quad \boldsymbol{\varepsilon}_{2}^{(k)} \quad \boldsymbol{\varepsilon}_{3}^{(k)} \quad \boldsymbol{\gamma}_{13}^{(k)} \quad \boldsymbol{\gamma}_{23}^{(k)} \quad \boldsymbol{\gamma}_{12}^{(k)} \right\}^{T} \equiv \left\{ \frac{\partial u_{1}}{\partial x_{1}} \quad \frac{\partial u_{2}}{\partial x_{2}} \quad \frac{\partial u_{3}}{\partial x_{3}} \quad \frac{\partial u_{1}}{\partial x_{3}} + \frac{\partial u_{3}}{\partial x_{1}} \quad \frac{\partial u_{2}}{\partial x_{2}} + \frac{\partial u_{3}}{\partial x_{2}} \quad \frac{\partial u_{1}}{\partial x_{2}} + \frac{\partial u_{2}}{\partial x_{1}} \right\}^{T} \quad (2b)$$

$$\boldsymbol{\varepsilon}^{(k)} = \boldsymbol{L}_{1} \cdot \boldsymbol{u} = \boldsymbol{L}_{1} \cdot \left\{ u_{1}^{(k)} \quad u_{2}^{(k)} \quad u_{3}^{(k)} \right\}^{T}; \quad \boldsymbol{L}_{1}^{T} = \begin{bmatrix} \frac{\partial}{\partial x_{1}} & 0 & 0 & \frac{\partial}{\partial x_{3}} & 0 & \frac{\partial}{\partial x_{2}} \\ 0 & \frac{\partial}{\partial x_{2}} & 0 & 0 & \frac{\partial}{\partial x_{3}} & \frac{\partial}{\partial x_{1}} \\ 0 & 0 & \frac{\partial}{\partial x_{3}} & \frac{\partial}{\partial x_{1}} & \frac{\partial}{\partial x_{2}} & 0 \end{bmatrix}$$
(2c)

$$\mathbf{E}^{(k)} = \left\{ E_1^{(k)} \quad E_2^{(k)} \quad E_3^{(k)} \right\}^T \equiv \left\{ -\frac{\partial \Phi_p^{(k)}}{\partial x_1} \quad -\frac{\partial \Phi_p^{(k)}}{\partial x_2} \quad -\frac{\partial \Phi_p^{(k)}}{\partial x_2} \right\}^T \tag{2d}$$

$$\boldsymbol{E}^{(k)} = \boldsymbol{L}_2.\,\boldsymbol{\Phi}_p^{(k)} \equiv \left\{ -\frac{\partial}{\partial x_1} - \frac{\partial}{\partial x_2} - \frac{\partial}{\partial x_3} \right\}^T \boldsymbol{\Phi}_p^{(k)} \tag{2e}$$

$$\mathbf{D}^{(k)} = \left\{ D_1^{(k)} \quad D_2^{(k)} \quad D_2^{(k)} \right\}^T \tag{2f}$$

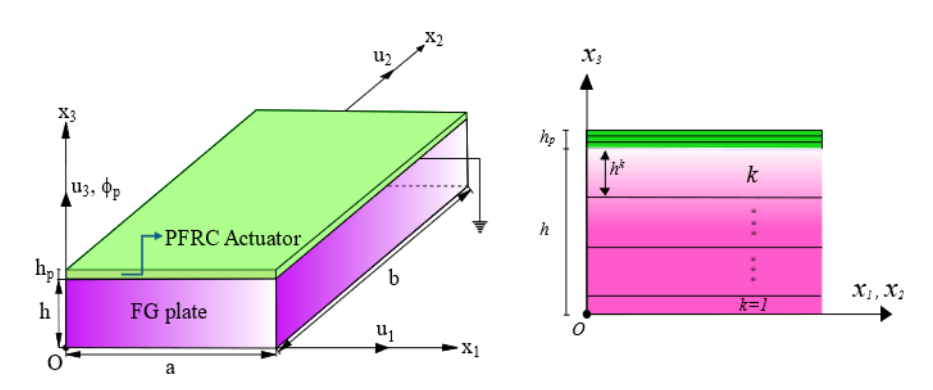


Fig. 1. Geometry and kinematic variables of the rectangular FG plate attached with a PFRC actuator at the top

where $\sigma^{(k)}$, $\boldsymbol{\mathcal{E}}^{(k)}$, $\boldsymbol{\mathcal{E}}^{(k)}$, and $\boldsymbol{\mathcal{D}}^{(k)}$ represent the stress, strain, electrical field and electrical displacement vectors, respectively. Herein, $\boldsymbol{\mathcal{\Phi}}_p^{(k)}$ stands for the electrical potential. If the kth lamina is made of an orthotropic material, transformed elastic material matrix, $\bar{\boldsymbol{\mathcal{Q}}}^{(k)}$ in Eq. (1) is symmetric and can be written as:

$$\begin{bmatrix} \bar{Q}_{11} & \bar{Q}_{12} & \bar{Q}_{13} & 0 & 0 & \bar{Q}_{16} \\ \bar{Q}_{12} & \bar{Q}_{22} & \bar{Q}_{23} & 0 & 0 & \bar{Q}_{26} \\ \bar{Q}_{13} & \bar{Q}_{23} & \bar{Q}_{33} & 0 & 0 & \bar{Q}_{36} \\ 0 & 0 & 0 & \bar{Q}_{44} & \bar{Q}_{45} & 0 \\ 0 & 0 & 0 & \bar{Q}_{45} & \bar{Q}_{55} & 0 \\ \bar{Q}_{16} & \bar{Q}_{26} & \bar{Q}_{36} & 0 & 0 & \bar{Q}_{66} \end{bmatrix}$$

$$(3)$$

Laminates are composed of multiple laminae, each of which can be oriented at any angle, $\theta^{(k)}$ relative to the laminate's reference system. Thereby, the local stiffness terms of each lamina, $Q_{ij}^{(k)}(\bar{\boldsymbol{x}}_i^{(k)})$ need to be transformed into global ones, $\bar{Q}_{ij}^{(k)}(\boldsymbol{x}_i^{(k)})$ (given in Eq. (3) to provide the alignment with the coordinates of the geometric problem, $\boldsymbol{x}_i^{(k)}$. For the sake of completeness, the explicit form of the transformation, $\bar{Q}_{ij}^{(k)}(\boldsymbol{x}_i^{(k)}) = f(Q_{ij}^{(k)}, \theta^{(k)})$ is given in Appendix A. The local stiffness terms of an orthotropic material, $Q_{ij}^{(k)}$ can be formulated in terms of engineering constants as follows:

$$Q_{11}^{(k)} = \frac{E_1^{(k)} (1 - \nu_{23}^{(k)} \nu_{32}^{(k)})}{\Lambda^{(k)}} \qquad Q_{12}^{(k)} = \frac{E_1^{(k)} (\nu_{21}^{(k)} + \nu_{31}^{(k)} \nu_{23}^{(k)})}{\Lambda^{(k)}} \qquad Q_{13}^{(k)} = \frac{E_3^{(k)} (\nu_{13}^{(k)} + \nu_{12}^{(k)} \nu_{23}^{(k)})}{\Lambda^{(k)}}$$
(4a)

$$Q_{22}^{(k)} = \frac{E_2^{(k)} (1 - v_{13}^{(k)} v_{31}^{(k)})}{\Lambda^{(k)}} \qquad Q_{23}^{(k)} = \frac{E_3^{(k)} (v_{23}^{(k)} + v_{21}^{(k)} v_{13}^{(k)})}{\Lambda^{(k)}} \qquad Q_{33}^{(k)} = \frac{E_3^{(k)} (1 - v_{12}^{(k)} v_{21}^{(k)})}{\Lambda^{(k)}}$$
(4b)

$$Q_{44}^{(k)} = G_{13}^{(k)} \qquad \qquad Q_{55}^{(k)} = G_{23}^{(k)} \qquad \qquad Q_{66}^{(k)} = G_{12}^{(k)} \qquad \qquad (4c)$$

$$\Delta^{(k)} = 1 - \nu_{12}^{(k)} \nu_{21}^{(k)} - \nu_{23}^{(k)} \nu_{32}^{(k)} - \nu_{31}^{(k)} \nu_{13}^{(k)} - 2\nu_{21}^{(k)} \nu_{32}^{(k)} \nu_{13}^{(k)}$$

$$\tag{4d}$$

If the kth lamina is isotropic and homogeneous in the x_1x_2 domain, while exhibiting non-homogeneity along the thickness- x_3 direction, akin to functionally graded materials, Eqs. (3-4) lead to:

$$\bar{Q}_{11}^{(k)} = Q_{11} = \bar{Q}_{22}^{(k)} = Q_{22} = \bar{Q}_{33}^{(k)} = Q_{33} = \frac{(1 - \nu)E(x_3)}{(1 + \nu)(1 - 2\nu)}$$
 (5a)

$$\bar{Q}_{12}^{(k)} = Q_{12} = \bar{Q}_{13}^{(k)} = Q_{13} = \bar{Q}_{23}^{(k)} = Q_{23} = \frac{\nu E(x_3)}{(1+\nu)(1-2\nu)}$$
 (5b)

$$\bar{Q}_{44}^{(k)} = Q_{44} = \bar{Q}_{55}^{(k)} = Q_{55} = \bar{Q}_{66}^{(k)} = Q_{66} = \frac{E(x_3)}{2(1+\nu)}$$
 (5c)

in which Poisson's ratio, ν is kept constant and Young's modulus of FG material, $E(x_3)$ can be governed by an exponential law through the thickness as:

$$E(x_3) = E_0 e^{\lambda x_3} \tag{6a}$$

where E_0 refers to the Young's modulus of the material located at the bottom surface of the FG plate and λ is a parameter that describes the gradient of inhomogeneity in the functionally graded material throughout the thickness. In a similar manner, transformed piezoelectricity, $\bar{e}^{(k)}$ and permittivity matrix, $\bar{\Lambda}^{(k)}$ terms defined in Eqs. (1a-b) can be rearranged having the following exponential distributions as:

$$\bar{e}_{ij}^{(k)} = 0 \quad \bar{e}_{ij}^{(1)} e^{\lambda x_3} \qquad \qquad \bar{\Lambda}_{ij}^{(k)} = 0 \quad \bar{\Lambda}_{ij}^{(1)} e^{\lambda x_3}$$
 (6b)

where $0\bar{t}_{ij}^{(1)}$; $(t = e, \Lambda)$ are the values at the plane $x_3 = 0$.

2.2. NURBS basis functions in isogeometric analysis

This section gives a brief introduction to B-splines and NURBS basis functions, which are employed to discretize the problem of geometry and kinematic variables [23, 24]. The knot vector, $U = \{\xi_1 \ \xi_2 \ \cdots \ \xi_i \ \cdots \ \xi_{n+p+1}\}$ consists of a non-decreasing series of real numbers within the parameter space, ξ where ξ_i representing the *i*th knot, *i* as the knot index, *n* being the total number of basic functions and *p* indicating the polynomial order. The B-spline basis functions [37] are defined recursively based on the Cox-De-Boor formula for p = 0 and any pth degree as:

$$N_i^0(\xi) = \begin{cases} 1 & if \xi_i \le \xi \le \xi_{i+1} \\ 0 & \text{otherwise} \end{cases}$$
 (7a)

$$N_i^p(\xi) = \frac{\xi - \xi_i}{\xi_{i+p} - \xi_i} N_i^{p-1}(\xi) + \frac{\xi_{i+p+1} - \xi}{\xi_{i+p+1} - \xi_{i+1}} N_{i+1}^{p-1}(\xi)$$
 (7b)

B-splines functions are nonnegative $(N_i^p(\xi) \ge 0)$ and have local support property that means for a given knot span and degree, i.e, ξ_i $\xi_{i+1}) = \xi_3$ ξ_4) and p = 2, the total number of nonzero B-splines functions are (p+1) = 3, that are $(N_{i-p}^p(\xi) \cdots \to N_i^p(\xi)) \equiv (N_1^2(\xi) \ N_2^2(\xi) \ N_3^2(\xi))$. While B-spline basis polynomials, constructed using Eqs. (7a-b), has numerous advantages, there are several important types of curves and surfaces that cannot be exactly represented by B-splines, including circles, ellipses, hyperbolas, cylinders, cones and spheres. It is a well-established fact that all these geometries need to be represented through rational functions, which are formed by the ratio of two polynomials. One (ζ) and two dimensional, (ξ, η) Non-Uniform Rational B-splines (NURBS) basis functions have been introduced for this purpose as follows:

$$\bar{R}_i^p(\zeta) = \frac{w_i N_i^p(\zeta)}{\sum_{i=1}^n w_i N_i^p(\zeta)}$$
(8a)

$$R_{ij}^{pq}(\xi,\eta) = \frac{w_{ij}N_i^p(\xi)M_j^q(\eta)}{\sum_{j=1}^m \sum_{i=1}^n w_{ij}N_i^p(\xi)M_j^q(\eta)}$$
(8b)

where w_i, w_{ij} are the associated weights and $M_j^q(\eta)$ represent the nonrational B-spline functions defined in the η -direction with a degree of q. The variable m refers to the total number of basic functions defined in the knot vector, $V = \{\eta_1 \ \eta_2 \ \cdots \ \eta_j \ \cdots \ \eta_{m+q+1}\}$. A nonzero $(\xi_i \neq \xi_{i+1} \land \eta_j \neq \eta_{j+1})$ knot span, $\xi_i, \xi_{i+1} \rangle \otimes \eta_j, \eta_{j+1})$ gives the domain of an isogeometric 2-D element, $\Omega^{(e)}$. Herein this knot span, the nonzero NURBS functions are constructed with nonzero Bsplines, that are $(N_{i-p}^p, N_{i-p+1}^p, \cdots N_i^p) \otimes (M_{j-q}^q, M_{j-q+1}^q, \cdots M_j^q)$ with a total number of $nen = (p+1) \times (q+1)$. $S(\xi, n)$ represents a NURBS surface and can be constructed using NURBS functions defined in Eq. (8) along with the control point coordinates matrix, $P_{ij} = \{x_{ij}, y_{ij}, z_{ij}\}^T$ in the following form:

$$S(\xi, n) = \{x_1(\xi, n) \mid x_2(\xi, n) \mid x_3(\xi, n)\}^T = \sum_{i=1}^m \sum_{j=1}^n R_{ij}^{pq}(\xi, \eta) \mathbf{P}_{ij}$$
(9)

Herein, the control points (except for the first and last ones) defined in P_{ij} matrix generally do not lie on the physical geometry (not interpolatory) that makes them distinct from the nodes in classical FEM analysis. Thereby, imposing boundary conditions in complex geometric forms of IGA is an issue that needs to be considered carefully.

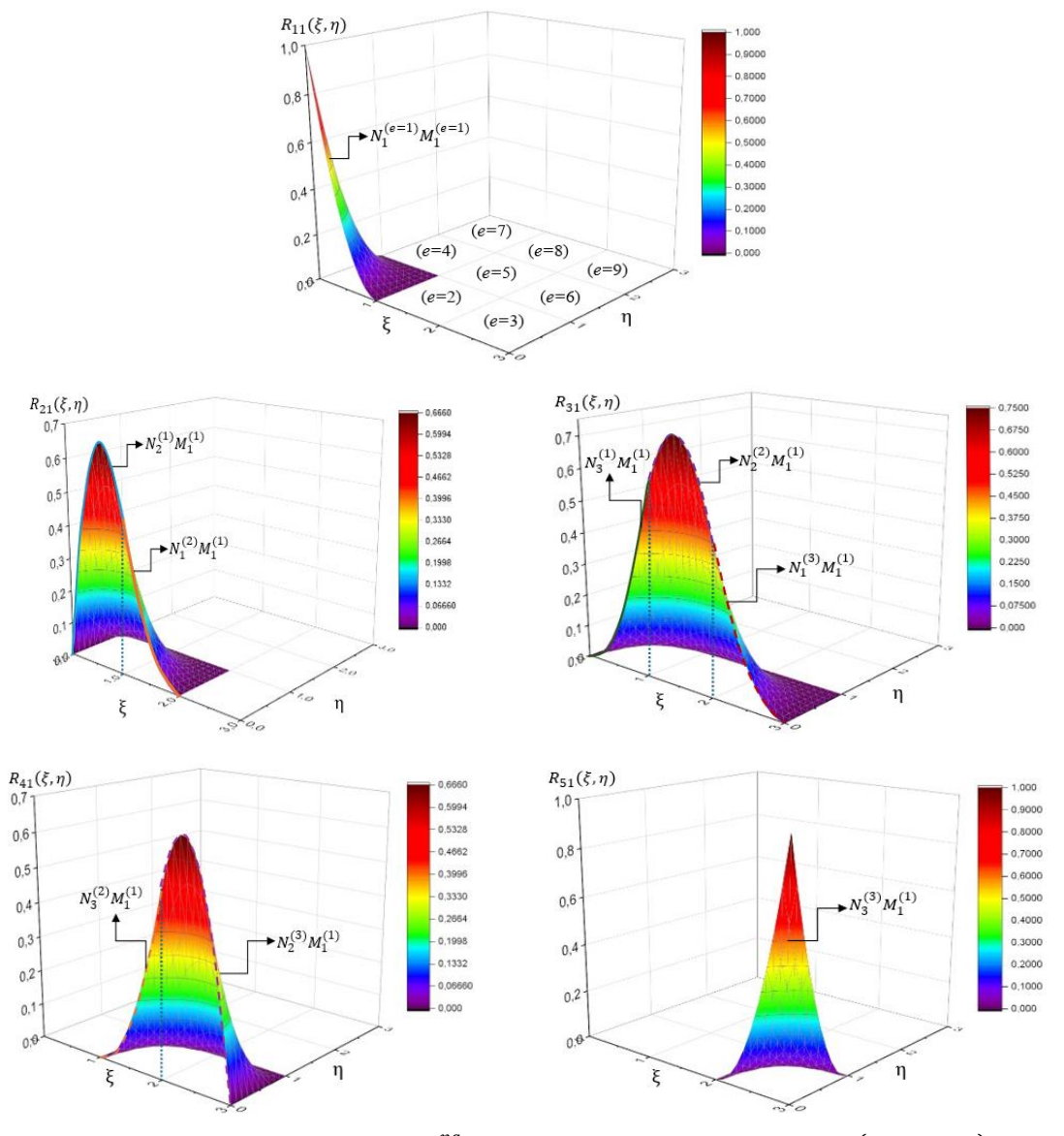


Fig. 2. The first five NURBS functions, $R_{ij}^{pq}(\xi,\eta)$ defined on 0,3) \otimes 0,1)knot domain $(w_{ij}$ s are 1.0)

2.3. Layerwise kinematics

Reddy's layerwise theory [39] is based on the idea of expressing the kinematic unknowns in the form of a two-part function, specifically in-plane, (x_1, x_2) and thickness directions, x_3 as:

$$\boldsymbol{U}(x_1, x_2, x_3) = \{u_1 \quad u_2 \quad u_3\}^T = \sum_{j=1}^N \bar{\boldsymbol{U}}^j(x_1, x_2) \bar{R}_j^p(x_3) \qquad \bar{\boldsymbol{U}}^j(x_1, x_2) = \{u_1^j \quad u_2^j \quad u_3^j\}^T \qquad (10)$$

where the in-plane variable functions, $\bar{U}^j(x_1, x_2)$ represent the displacements of all points located on the *j*th plane, $(x_3 = x_3^j)$. Herein, $\bar{R}_j^p(x_3)$ refers to the 1D NURBS functions through the thickness coordinate. In a similar manner, the in-plane variable functions can be discretized utilizing 2D NURBS functions as:

$$\bar{\boldsymbol{U}}^{j}(x_{1}, x_{2}) = \sum_{i=1}^{M} \hat{\mathbf{U}}^{ji} R_{i}^{pq}(x_{1}, x_{2}) \qquad \qquad \hat{\mathbf{U}}^{ji} = \left\{ u_{1}^{ji} \quad u_{2}^{ji} \quad u_{3}^{ji} \right\}^{T}$$
(11)

By expressing the equations for the unknown displacements written above in matrix form and elementwise, it would be as follows:

$${\overset{(ez)}{(e)}}\boldsymbol{u}(x_1,x_2,x_3) = {\overset{(ez)}{(e)}}u_1 \quad {\overset{(ez)}{(e)}}u_2 \quad {\overset{(ez)}{(e)}}u_3 {\overset{(ez)}{(e)}}\boldsymbol{R}_z(x_3(\zeta)). \quad {\overset{(ez)}{(e)}}\boldsymbol{R}_{xy}(x_1(\xi,\eta),x_2(\xi,\eta)). \quad \widehat{\overset{(ez)}{(e)}}\boldsymbol{u}$$
 (12)

$${}^{(ez)}_{(e)}R_{xy}(\xi,\eta) = \begin{bmatrix} R^1_{xy}(\xi,\eta) & \mathbf{0} & \mathbf{0} & \mathbf{0} \\ \mathbf{0} & R^j_{xy}(\xi,\eta) & \mathbf{0} & \mathbf{0} \\ \mathbf{0} & \mathbf{0} & \ddots & \mathbf{0} \\ \mathbf{0} & \mathbf{0} & \mathbf{0} & R^{nenz}_{xy}(\xi,\eta) \end{bmatrix}$$
(13a)

$$\mathbf{R}_{xy}^{j}(\xi,\eta) = \begin{bmatrix} {}^{1}\mathbf{R}_{xy}^{j} & {}^{i}\mathbf{R}_{xy}^{j} & \cdots & {}^{nen}\mathbf{R}_{xy}^{j} \end{bmatrix} \qquad {}^{i}\mathbf{R}_{xy}^{j} = \begin{bmatrix} R_{i}^{(e)}(\xi,\eta) & 0 & 0 \\ 0 & R_{i}^{(e)}(\xi,\eta) & 0 \\ 0 & 0 & R_{i}^{(e)}(\xi,\eta) \end{bmatrix}$$
(13b)

$$\widehat{\boldsymbol{u}}_{(e)} = [\widehat{\boldsymbol{u}}_1 \quad \widehat{\boldsymbol{u}}_2 \quad \cdots \quad \widehat{\boldsymbol{u}}_j \quad \cdots \quad \widehat{\boldsymbol{u}}_{nenz}]^T \quad \widehat{\boldsymbol{u}}_j = [u_1^{j_1} \quad u_2^{j_1} \quad u_3^{j_1} \quad u_1^{j_2} \quad u_3^{j_2} \quad u_3^{j_2} \quad \cdots \quad u_1^{j_{nen}} \quad u_2^{j_{nen}} \quad u_3^{j_{nen}}]^T \quad (13c)$$

where nenz = pz + 1 with the NURBS degree of pz through the thickness coordinate, ζ . The indices, e and ez correspond to the elements in the x_1x_2 plane and x_3 directions, respectively. In a similar manner, the electrical potential in an $(ez, e)^{th}$ element can be discretized as:

$$\stackrel{(ez)}{_{(e)}} \boldsymbol{\phi}_{p}^{(k)} = \stackrel{\widetilde{(ez)}}{_{(e)}} \boldsymbol{R}_{z} \stackrel{\widetilde{(ez)}}{_{(e)}} \boldsymbol{\pi}_{xy} \stackrel{\widetilde{(ez)}}{_{(e)}} \boldsymbol{\phi}_{p}$$
 (14a)

where

$$\underbrace{\widetilde{(ez)}}_{(e)} \widetilde{R}_{xy}(\xi, \eta) = \begin{bmatrix}
\widetilde{R}_{xy}^{1} & 0 & 0 & 0 & 0 & 0 \\
0 & \widetilde{R}_{xy}^{2} & 0 & 0 & 0 & 0 \\
0 & 0 & \ddots & 0 & 0 & 0 \\
0 & 0 & 0 & \widetilde{R}_{xy}^{j} & 0 & 0 \\
0 & 0 & 0 & 0 & \ddots & 0 \\
0 & 0 & 0 & 0 & \widetilde{R}_{xy}^{nenz}
\end{bmatrix} \qquad \widetilde{R}_{xy}^{j} = \begin{bmatrix}
R_{1}^{(e)} & R_{2}^{(e)} & \cdots & R_{nen}^{(e)}
\end{bmatrix} \qquad (14b)$$

$$\begin{array}{ll}
\overbrace{(e)}^{(e)} \mathbf{R}_z(\zeta) = \begin{bmatrix} \bar{R}_z^1(\zeta) & \bar{R}_z^2(\zeta) & \bar{R}_z^j(\zeta) & \cdots & \bar{R}_z^{nenz}(\zeta) \end{bmatrix} \\
\end{array} (14c)$$

The virtual work, $\binom{(ez)}{(e)} \delta U$ done by the internal force and electrical displacements in moving through virtual displacement and electrical potential can be expressed as:

$$\int_{0}^{(ez)} \delta U = \iint_{0}^{e} \int_{h^{ez}} \left((\delta \boldsymbol{\varepsilon}^{(k)})^{T} \boldsymbol{\sigma}^{(k)} - (\delta \boldsymbol{E}^{(k)})^{T} \boldsymbol{D}^{(k)} \right) dx_{3} dx_{1} dx_{2}$$
(15)

By replacing the constitutive equations, Eqs. (1a-b) for $\sigma^{(k)}$ and $D^{(k)}$ into Eq. (15) gives:

$$\int_{0}^{(ez)} \delta U = \iint_{0}^{e} \int_{k^{ez}} \left((\delta \boldsymbol{\varepsilon}^{(k)})^T \bar{\boldsymbol{Q}}^{(k)} \boldsymbol{\varepsilon}^{(k)} - (\delta \boldsymbol{\varepsilon}^{(k)})^T \bar{\boldsymbol{e}}^{(k)} \boldsymbol{E}^{(k)} - (\delta \boldsymbol{E}^{(k)})^T \bar{\boldsymbol{e}}^{(k)} \boldsymbol{\varepsilon}^{(k)} - (\delta \boldsymbol{E}^{(k)})^T \bar{\boldsymbol{A}}^{(k)} \boldsymbol{E}^{(k)} \right) dx_3 dx_1 dx_2$$
 (16)

From this point on, the indices, e and ez will not be displayed in the terms unless undeemed necessary for the purpose of simplifying equations. The following strain energy variation can be obtained via substituting Eqs. (2c-e) into Eq. (16) respectively for $\varepsilon^{(k)}$ and $\varepsilon^{(k)}$ and $\varepsilon^{(k)}$ yields:

$$\iint_{\Omega^{e}} \int_{h^{ez}} \left[(\delta \mathbf{u})^{T} \mathbf{L}_{1}^{T} \bar{\mathbf{Q}}^{(k)} \mathbf{L}_{1} \mathbf{u} - (\delta \mathbf{u})^{T} \mathbf{L}_{1}^{T} \bar{\mathbf{e}}^{(k)} \mathbf{L}_{2} \Phi_{p}^{(k)} - (\delta \Phi_{p}^{(k)})^{T} \mathbf{L}_{2}^{T} \bar{\mathbf{e}}^{(k)} \mathbf{L}_{1} \mathbf{u} - (\delta \Phi_{p}^{(k)})^{T} \mathbf{L}_{2}^{T} \bar{\mathbf{A}}^{(k)} \mathbf{L}_{2} \Phi_{p}^{(k)} \right] dx_{3} dx_{1} dx_{2}$$
(17)

Furthermore, the displacement and electrical potential vectors in Eq. (17) can be expressed in terms of the discretized forms presented in Eqs. (12-14a), the resulting final form of Eq. (17) will be:

$$(ez) \delta U = \iint_{\Omega^e} \int_{h^{ez}} \left[\underbrace{(\delta \widehat{\boldsymbol{u}})^T \underbrace{R_{\boldsymbol{xy}}^T \bar{R}_{\boldsymbol{z}}^T L_{1}^T}_{(B_{\boldsymbol{u}})^T} \bar{\boldsymbol{Q}}^{(k)} \underbrace{L_{1} \bar{R}_{\boldsymbol{z}} R_{\boldsymbol{xy}}}_{B_{\boldsymbol{u}}} \widehat{\boldsymbol{u}} - (\delta \widehat{\boldsymbol{u}})^T \underbrace{R_{\boldsymbol{xy}}^T \bar{R}_{\boldsymbol{z}}^T L_{1}^T}_{(B_{\boldsymbol{u}})^T} \bar{\boldsymbol{e}}^{(k)} \underbrace{L_{2} \tilde{R}_{\boldsymbol{z}} \tilde{R}_{\boldsymbol{xy}}}_{B_{\boldsymbol{\phi}}} \widehat{\boldsymbol{\Phi}}_{\boldsymbol{p}} - (\delta \widehat{\boldsymbol{\Phi}}_{\boldsymbol{p}})^T \underbrace{\tilde{R}_{\boldsymbol{xy}}^T \bar{R}_{\boldsymbol{z}}^T L_{2}^T}_{(B_{\boldsymbol{\phi}})^T} \bar{\boldsymbol{e}}^{(k)} \underbrace{L_{1} \bar{R}_{\boldsymbol{z}} R_{\boldsymbol{xy}}}_{B_{\boldsymbol{u}}} \widehat{\boldsymbol{u}} - (\delta \widehat{\boldsymbol{\Phi}}_{\boldsymbol{p}})^T \underbrace{\tilde{R}_{\boldsymbol{xy}}^T \bar{R}_{\boldsymbol{z}}^T L_{2}^T}_{(B_{\boldsymbol{\phi}})^T} \bar{\boldsymbol{A}}^{(k)} \underbrace{L_{2} \tilde{R}_{\boldsymbol{z}} \tilde{R}_{\boldsymbol{xy}}}_{B_{\boldsymbol{\phi}}} \widehat{\boldsymbol{\Phi}}_{\boldsymbol{p}} \right] dx_3 dx_1 dx_2$$

$$(18)$$

For the sake of completeness, B_u and B_{Φ} appeared in Eq. (18) are given in the Appendix B. Note that the element strain-displacement and potential-displacement matrices, B_u , B_{Φ} , given in Eqs. (B1-B2) contain not only NURBS functions but also derivatives. To obtain the NURBS derivatives with respect to physical in-plane coordinates, (x_1, x_2) , one must apply the chain rule in the form:

$$\begin{bmatrix}
\frac{\partial R_{ij}}{\partial x_1} \\
\frac{\partial R_{ij}}{\partial x_2}
\end{bmatrix}^{(e)} = \begin{bmatrix}
\frac{\partial \xi}{\partial x_1} & \frac{\partial \eta}{\partial x_1} \\
\frac{\partial \xi}{\partial x_2} & \frac{\partial \eta}{\partial x_2}
\end{bmatrix}^{(e)} \begin{bmatrix}
\frac{\partial R_{ij}}{\partial \xi} \\
\frac{\partial R_{ij}}{\partial \eta}
\end{bmatrix}^{(e)} \equiv (J_1^{-1})^{(e)} \left(\mathbf{R}_{der}^{\xi\eta}\right)^{(e)} \tag{19}$$

where $(J_1^{-1})^{(e)}$ represents the inverse of the element Jacobian matrix, $J_1^{(e)}$. With the aid of known control point coordinates, $(x_1^{ij}, x_2^{ij})^{(e)}$ and the NURBS basis functions, $R_{ij}^{(e)}(\xi, \eta) \equiv R_I^{(e)}(\xi, \eta)$; the mapping between the physical in-plane, $\Omega^{(e)}(x_1, x_2)$ and parametric domains of an eth element, $\hat{\Omega}^{(e)}(\xi, \eta)$ can be accomplished by a similar approach defined in Eq. (28) as:

$$x_{1}^{(e)} = \sum_{i=1}^{(p+1)} \sum_{j=1}^{(e+1)} \sum_{i=1}^{(e)} x_{1}^{ij} R_{ij}^{(e)}(\xi, \eta) \equiv \sum_{I=1}^{nen} x_{1}^{I} R_{I}^{(e)} \qquad x_{2}^{(e)} = \sum_{i=1}^{(p+1)} \sum_{j=1}^{(e)} \sum_{i=1}^{(e)} x_{2}^{ij} R_{ij}^{(e)}(\xi, \eta) \equiv \sum_{I=1}^{nen} x_{2}^{I} R_{I}^{(e)} \qquad (20)$$

Thus, the inverse of the element Jacobian matrix, $J_1^{(e)}$ required in Eq. (19), can be evaluated by taking the derivatives of Eqs. (20) with respect to parametric coordinates, (ξ, η) that yields the $J_1^{(e)}$ to be obtained as:

$$J_{1}^{(e)} = \begin{bmatrix} \frac{\partial x_{1}}{\partial \xi} & \frac{\partial x_{2}}{\partial \xi} \\ \frac{\partial x_{1}}{\partial \eta} & \frac{\partial x_{2}}{\partial \eta} \end{bmatrix}^{(e)} \equiv \begin{bmatrix} \frac{\partial R_{1}}{\partial \xi} & \frac{\partial R_{2}}{\partial \xi} & \dots & \frac{\partial R_{nen}}{\partial \xi} \\ \frac{\partial R_{1}}{\partial \eta} & \frac{\partial R_{2}}{\partial \eta} & \dots & \frac{\partial R_{nen}}{\partial \eta} \end{bmatrix}^{(e)} \begin{bmatrix} x_{1}^{1} & x_{2}^{1} \\ x_{1}^{2} & x_{2}^{2} \\ \vdots & \vdots \\ x_{1}^{nen} & x_{2}^{nen} \end{bmatrix}^{(e)}$$
(21)

Also, the Jacobian term, $J_2^{(ez)}$ of the transformation between the physical and parametric thickness coordinates, (x_3, ζ) can be written as:

$$J_{2}^{(ez)} = \left(\frac{dx_{3}}{d\zeta}\right)^{(ez)} \equiv \left\{\frac{d\bar{R}_{z}^{1}}{d\zeta} \quad \frac{d\bar{R}_{z}^{2}}{d\zeta} \quad \cdots \quad \frac{d\bar{R}_{z}^{nenz}}{d\zeta}\right\}^{(ez)} \left\{\begin{array}{c} x_{3}^{1} \\ x_{3}^{2} \\ \vdots \\ x_{3}^{nenz} \end{array}\right\}^{(ez)}$$
(22)

The difficulty of integrating Eq. (18) analytically gives rise to the numerical Gauss-Legendre quadrature method that needs a further mapping from parametric coordinates, (ξ, η, ζ) to parent element space, $(\xi, \tilde{\eta}, \tilde{\zeta})$ as:

$$\xi = \xi_i + (\tilde{\xi} + 1) \frac{(\xi_{i+1} - \xi_i)}{2} \quad \eta = \eta_j + (\tilde{\eta} + 1) \frac{(\eta_{j+1} - \eta_j)}{2}; \quad \zeta = \zeta_k + (\bar{\zeta} + 1) \frac{(\zeta_{k+1} - \zeta_k)}{2} \quad (23a)$$

$${(ez) \choose (e)} J_3 = \frac{d\xi}{d\tilde{\xi}} \frac{d\eta}{d\tilde{\eta}} \frac{d\zeta}{d\tilde{\zeta}} \equiv \frac{(\xi_{i+1} - \xi_i)}{2} \frac{(\eta_{j+1} - \eta_j)}{2} \frac{(\zeta_{k+1} - \zeta_k)}{2}$$
(23b)

Furthermore, additional relations that will be needed in Eq. (18) is:

$$dx_1 dx_2 = |J_1^{(e)}| d\xi d\eta dx_3 = J_2^{(ez)} d\zeta (24)$$

where $|J_1^{(e)}|$ stands for the determinant of the Jacobian matrix and interested readers are referred to [40] for the proof of the relations. By applying the transformations, the element virtual work integral can be rewritten as:

where J represents the total Jacobian that can be computed as:

$$J = \left| \mathbf{J}_{1}^{(e)} \right| \times J_{2} \times J_{3} \tag{26}$$

The element stiffness matrix terms of Eq. (25) can be separated and computed as:

$${(ez) \choose (e)} \mathbf{K}_{uu} = \int_{-1}^{1} \int_{-1}^{1} \left(\int_{-1}^{1} (\mathbf{B}_{u})^{T} \bar{\mathbf{Q}}^{(k)} \mathbf{B}_{u} J d\tilde{\zeta} \right) d\tilde{\xi} d\tilde{\eta} \approx \sum_{r=1}^{N_{GP\zeta}} \sum_{s=1}^{N_{GP\zeta}} \left(\sum_{t=1}^{N_{GP\zeta}} \left((\mathbf{B}_{u})^{T} \bar{\mathbf{Q}}^{(k)} \mathbf{B}_{u} J \right) \Big|_{(\tilde{\zeta}_{t})} W_{t} \right) \right|_{(\tilde{\zeta}_{t})} W_{t} W_{s}$$
 (27a)

$${(ez) \choose (e)} K_{u\phi} = \int_{-1}^{1} \int_{-1}^{1} \left(\int_{-1}^{1} (\boldsymbol{B}_{u})^{T} \bar{\boldsymbol{e}}^{(k)} \boldsymbol{B}_{\boldsymbol{\phi}} J d\tilde{\boldsymbol{\zeta}} \right) d\tilde{\boldsymbol{\xi}} d\tilde{\boldsymbol{\eta}} \approx \sum_{r=1}^{N_{GP\zeta}} \sum_{s=1}^{N_{GP\zeta}} \left(\sum_{t=1}^{N_{GP\zeta}} \left((\boldsymbol{B}_{u})^{T} \bar{\boldsymbol{e}}^{(k)} \boldsymbol{B}_{\boldsymbol{\phi}} J \right) \Big|_{(\tilde{\boldsymbol{\zeta}}_{t}, \tilde{\boldsymbol{\eta}}_{s})} W_{t} W_{s}$$
 (27b)

$${(ez)\choose (e)}K_{\phi u} = \int_{-1}^{1}\int_{-1}^{1}\left(\int_{-1}^{1}(\boldsymbol{B}_{\phi})^{T}\bar{\boldsymbol{e}}^{(k)}\boldsymbol{B}_{u}Jd\tilde{\zeta}\right)d\tilde{\xi}d\tilde{\eta} \approx \sum_{r=1}^{N_{GP\bar{\eta}}}\sum_{s=1}^{N_{GP\bar{\eta}}}\left(\sum_{t=1}^{N_{GP\bar{\eta}}}\left((\boldsymbol{B}_{\phi})^{T}\bar{\boldsymbol{e}}^{(k)}\boldsymbol{B}_{u}J\right)\big|_{(\tilde{\zeta}_{t})}W_{t}\right)\bigg|_{(\tilde{\xi}_{r},\tilde{\eta}_{s})}W_{r}W_{s}$$
 (27c)

$${(ez)\choose (e)}K_{\phi\phi} = \int_{-1}^{1} \int_{-1}^{1} \left(\int_{-1}^{1} (\boldsymbol{B}_{\phi})^{T} \bar{\boldsymbol{\Lambda}}^{(k)} \boldsymbol{B}_{\phi} J d\tilde{\boldsymbol{\zeta}} \right) d\tilde{\boldsymbol{\xi}} d\tilde{\boldsymbol{\eta}} \approx \sum_{r=1}^{N_{GP\xi}} \sum_{s=1}^{N_{GP\xi}} \left(\sum_{t=1}^{N_{GP\xi}} \left((\boldsymbol{B}_{\phi})^{T} \bar{\boldsymbol{\Lambda}}^{(k)} \boldsymbol{B}_{\phi} J \right) \Big|_{\tilde{\boldsymbol{\xi}}_{\tau}, \tilde{\boldsymbol{\eta}}_{c}} W_{r} W_{s}$$
(27d)

where $^{(ez)}_{(e)}K_{uu}$ is the element mechanical stiffness matrix, $^{(ez)}_{(e)}K_{u\phi} = \binom{(ez)}{(e)}K_{\phi u}$ are the element piezoelectric matrix, and $^{(ez)}_{(e)}K_{\phi\phi}$ is the element electrical permittivity matrix. The number of in-plane Gauss points are denoted by $(N_{GP\xi}, N_{GP\eta})$ and taken as $(p+1) \times (q+1)$. Similarly, the number of thickness Gauss points, $N_{GP\zeta}$ are set to be pz+1 and W_r, W_s , and, W_t are the corresponding weights. In the absence of body forces, the virtual work done by the external mechanical forces and applied electric charges for an arbitrary variation of displacement field, $^{(ez)}_{(e)}\delta u$ and electric potential, $^{(ez)}_{(e)}\delta \phi_p^{(k)}$ can be written as:

$${(ez) \choose (e)} \delta W = \int_{(ez) \atop (e)} \left((\delta \boldsymbol{u})^T \boldsymbol{f}_s - \delta \boldsymbol{\Phi}_p^T q \right) dS$$
(28)

where f_s and q are the surface traction and charge vectors, respectively. By substituting Eqs. (12-14a) into Eq. (28) for $(\delta \mathbf{u})^T$ and $\delta \Phi_p^T$, one can obtain the element force vectors due to applied traction and surface charge as:

$${\substack{(ez)\\(e)}} \mathbf{F}_{s} = \int_{\substack{(ez)\\(e)}} \mathbf{R}_{xy}^{T} \tilde{\mathbf{R}}_{z}^{T} \mathbf{f}_{s} dS \qquad \qquad {\substack{(ez)\\(e)}} \mathbf{F}_{\phi} = -\int_{\substack{(ez)\\(e)}} \widetilde{\mathbf{R}}_{xy}^{T} \widetilde{\mathbf{R}}_{z}^{T} q dS \qquad (29)$$

Based on the principle that the actual displacement and electric potential vector minimize the potential energy function, $\delta E = \delta U - \delta W = 0$ the following element equations system is derived:

$$\begin{bmatrix}
K_{uu} & K_{u\phi} \\
K_{\phi u} & K_{\phi\phi}
\end{bmatrix} \begin{Bmatrix} \widehat{\boldsymbol{Q}}_{p} \end{Bmatrix}_{(e)}^{(ez)} = \begin{Bmatrix} F_{s} \\
F_{\phi} \end{Bmatrix}_{(e)}^{(ez)}$$
(30)

Following the similar element assembly procedure used in classic finite elements, global systems of equations are obtained, and the primary unknowns can be solved as:

$$\begin{Bmatrix} \hat{\boldsymbol{u}} \\ \hat{\boldsymbol{\Phi}}_{\boldsymbol{p}} \end{Bmatrix} = \begin{bmatrix} K_{uu} & K_{u\phi} \\ K_{\phi u} & K_{\phi \phi} \end{bmatrix}^{-1} \begin{Bmatrix} \boldsymbol{F}_{s} \\ \boldsymbol{F}_{\phi} \end{Bmatrix}$$
(31)

To make FGL-IGA more versatile and cost effective, the skyline solver algorithm has been utilized in the solution process. Thereby, only the terms on the upper diagonal part of the stiffness matrix have been focused, considering only the terms up to the last non-zero term in any given column, while disregarding the remaining zero terms above. An interested reader can refer to [40,41] on the skyline solver algorithm. Once the model unknowns, \hat{u} and $\hat{\Phi}_p$ are yielded, the expressions for $\varepsilon^{(k)}$, $\sigma^{(k)}$, $E^{(k)}$, and $D^{(k)}$ can be obtained from the strain-displacement and constitutive equations.

3. Numerical results

In this section, the numerical results are evaluated utilizing the FGL-IGA element derived in the preceding section. Two separate cases with analytical solutions available in literature have been selected. The first case aims to investigate the stress and displacement results of a plate made entirely of piezoelectric material with a functionally graded thickness under mechanical loads using FGL-IGA, while the second case aims to analyze the combined effects of electrical and mechanical loads by placing a piezoelectric layer on top of a functionally graded isotropic substrate layer. Assuming linear piezoelastic material behavior and small-strain, small-displacement conditions, the piezoelectric layers are subjected to mechanical and/or electrical loads and are perfectly bonded to each other. Furthermore, the shear-lag effect is ignored by neglecting the thickness of the adhesive between the layers.

Case 1

The first case, investigated by Zhong and Shang [17], features a square (a = b = 1 m) moderately thick plate, (a/h = 10) that is made entirely of piezoelectric material (PZT-4 at $x_3 = 0$) and functionally graded through its thickness. The state space approach has been applied in, and the corresponding approach is based on eliminating the five unknowns $(\sigma_{11}, \sigma_{22}, \sigma_{12}, D_1, D_2)$ from the governing piezoelectric field equations [17]. Thus, a total of eight unknowns $(u_1, u_2, \sigma_{33}, D_3, \sigma_{13}, \sigma_{23}, u_3, \varphi_p)$ can be obtained by utilizing eight boundary conditions to be applied to the simply supported plate. The elastic and piezoelectric properties of PZT-4 are given in Table 1. The static analysis of the FG piezoelectric plate under bisinusoidal mechanical loading, $q(x_1, x_2, x_3 = h) = q_0 \sin\left(\frac{\pi x_1}{a}\right) \sin\left(\frac{\pi x_2}{b}\right)$ with $q_0 = 1 \text{ N/m}^2$ has been conducted by modifying the material property gradient index, α in the range of (-1.0,1.0) that is utilized in the following material exponential distributions as:

$$\bar{Q}_{ij} = \bar{Q}_{ij}^0 e^{\alpha(x_3/h)} \qquad \qquad \bar{e}_{ij} = \bar{e}_{ij}^0 e^{\alpha(x_3/h)} \qquad \qquad \bar{\Lambda}_{ij} = \bar{\Lambda}_{ij}^0 e^{\alpha(x_3/h)}$$
(32)

where \bar{Q}_{ij}^0 , \bar{e}_{ij}^0 , and $\bar{\Lambda}_{ij}^0$ are the elastic stiffness, piezoelectric and dielectric tensor values at the plane, $x_3 = 0$. To obtain the desired accuracy, the in-plane and thickness domains are discretized into 14×14 and 6 quadratics, (p = q = pz = 2) isogeometric elements, respectively (Fig. 3). FGPM plate is simply supported and grounded on its four lateral edges that can be mathematically stated as:

$$u_2 = u_3 = \phi_p = 0$$
 at $x_1 = 0$ and a $u_1 = u_3 = \phi_p = 0$ at $x_2 = 0$ and b (33a)

$$\phi_p(x_1, x_2, x_3 = 0) = \phi_p(x_1, x_2, x_3 = h) = 0$$
(33b)

Table 1. Elastic and piezoelectric properties for PZT-4 and PZT-5H

	Elastic Proper	ties	F	Piezoelectric Proper	rties
Properties	PZT-4	PZT-5H	Properties	PZT-4	PZT-5H
$Q_{11}[GPa]$	139	32.6	$e_{31}[C/m^2]$	-5.2	-6.76
$Q_{22}[GPa]$	139	7.2	$e_{32}[C/m^2]$	-5.2	
$Q_{33}[GPa]$	115	7.2	$e_{33}[C/m^2]$	15.1	
$Q_{13}[GPa]$	74.3	4.76	$e_{24}[C/m^2]$	12.7	
$Q_{23}[GPa]$	74.3	3.85	$e_{15}[C/m^2]$	12.7	
$Q_{12}[GPa]$	77.8	4.3	$\varepsilon_{11}[F/m]$	$1475{\varepsilon_0}^*$	$4.179{\varepsilon_0}^*$
$Q_{44}[GPa]$	25.6	1.29	$\varepsilon_{22}[F/m]$	$1475{\varepsilon_0}^*$	$4.179{\varepsilon_0}^*$
$Q_{55}[GPa]$	25.6	1.05	$\varepsilon_{33}[F/m]$	$1300{\varepsilon_0}^*$	$1201.69\varepsilon_0{}^*$
$Q_{66}[GPa]$	30.6	1.29			

^{*}The vacuum dielectric constant used as $\varepsilon_0 = 8.854187817 \times 10^{-12} [F/m]$.

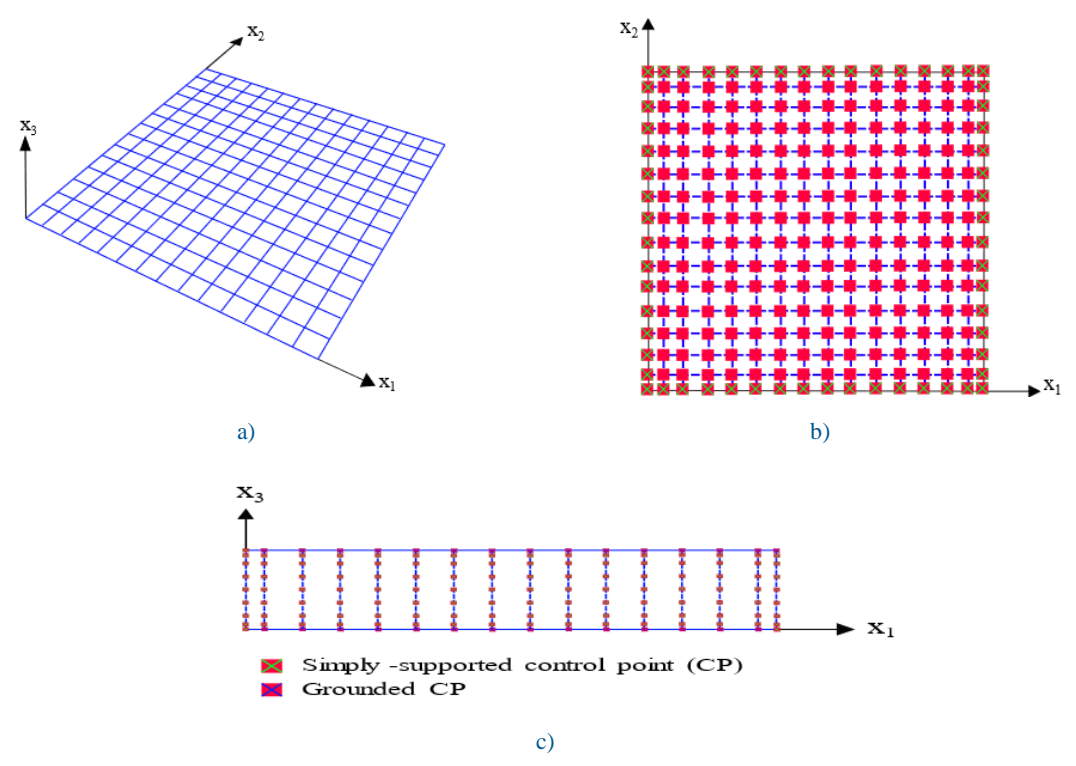


Fig. 3. Isogeometric discretization (14×14×6) of a square piezoelectric functionally graded plate with a fully simply supported boundary: Meshes of a) physical; b) in-plane CP; and c) transverse plane CP

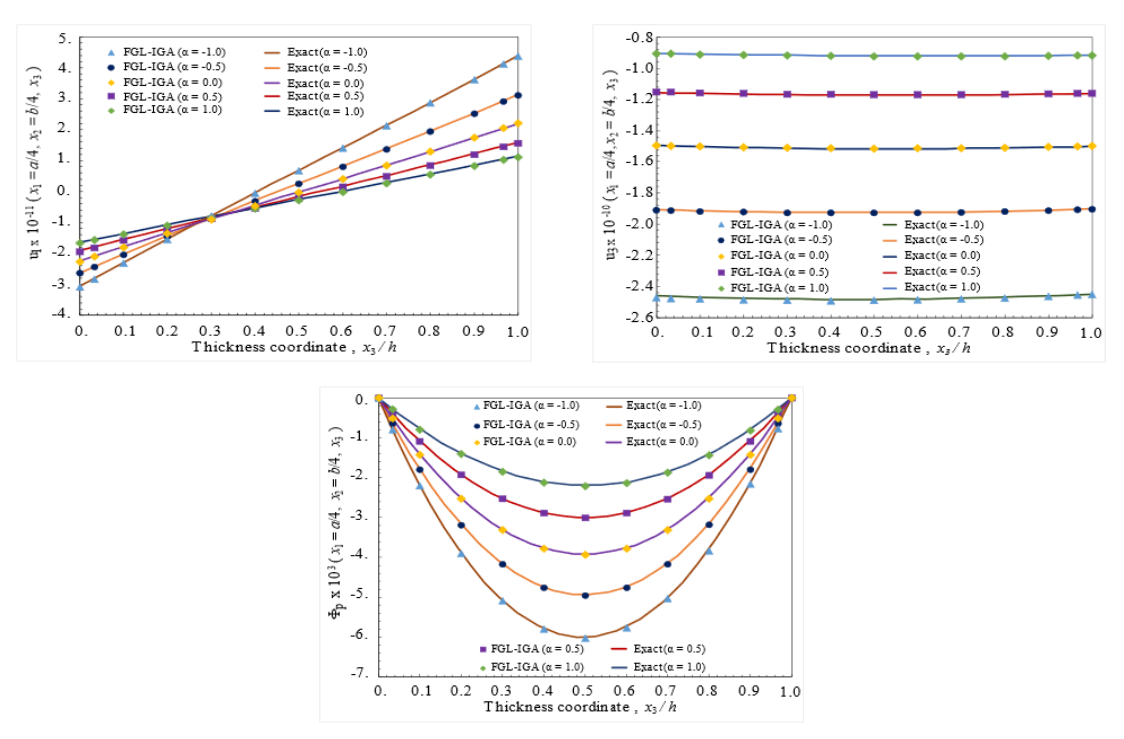


Fig. 4. Through-the-thickness displacement and electric potential variations

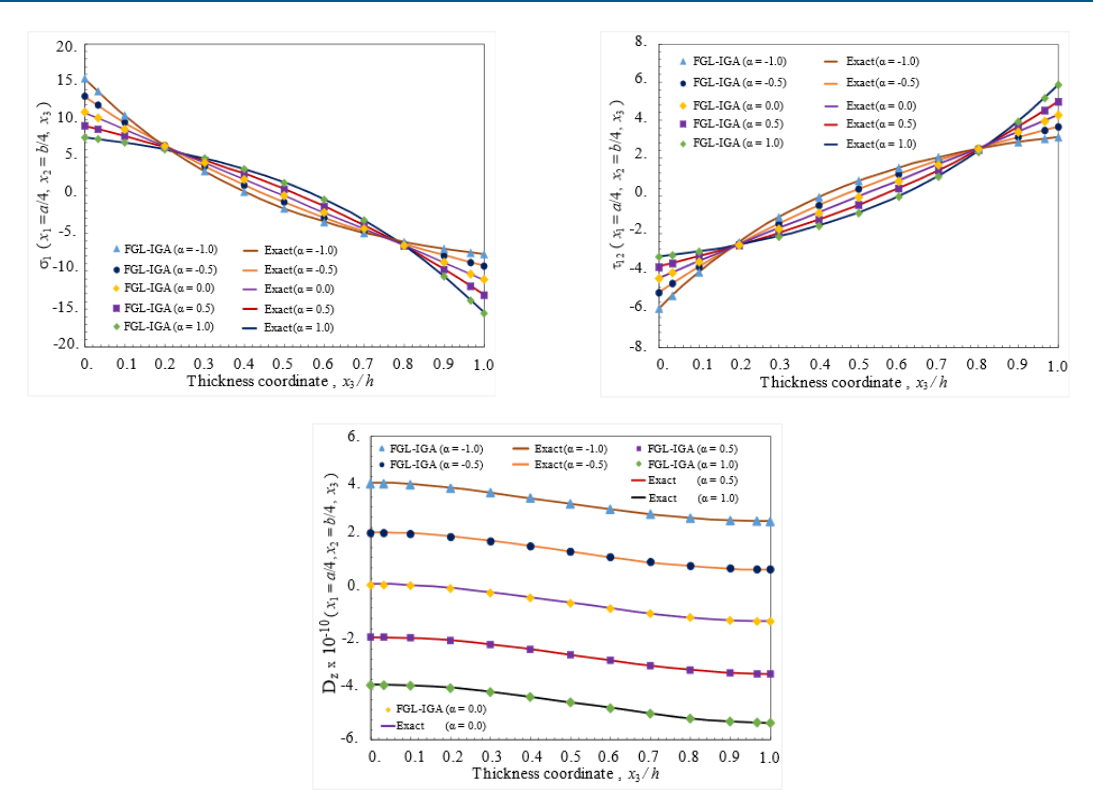


Fig. 5. Through-the-thickness stress and electric displacement variations

Fig. 4 illustrates the effect of the material gradient index, α on the distribution of in-plane and transverse displacements throughout the thickness of the functionally graded piezoelectric material (FGPM) plate, along with the electric potential. As exhibited in Fig. 4, when compared to the case where the material is homogeneous (PZT4 - α = 0) along the plate thickness, the positive values in the gradient index (α) leads to a reduction in the center deflection and electric potential as well as the in-plane displacements at the base (x_3 = 0). Additionally, while the effects of the negative values of the gradient index are in the opposite direction, it is evident from Fig. 4 that the rate of increase of these effects is higher for the negative values of the index compared to the positive ones. As depicted in Fig. 5, through-the-thickness in-plane normal and shear stress as well as transverse electrical displacement distributions obtained from FGL-IGA agree well with the analytical solution [17]. Herein, in-plane normal and shear stresses for α = 0 are in a linear form whereas the modification of gradient index makes the distributions exhibit a nonlinear pattern.

Case 2

Unlike the first case, herein, the second problem involves a square (a = b = 0.3 m) plate where a piezoelectric fiber-reinforced composite (PFRC) layer is placed on top, while a substrate layer made of functionally graded isotropic material is positioned beneath it (Fig. 1). By keeping the ratio $E_h/E_0 = 10$ constant, linear static analyses were performed over a wide range of the span/thickness ratio from a/h = 20 to 100, with both voltage and sinusoidal mechanical loadings applied to the top piezoelectric layer. The resulting displacement and stress values were then compared with the analytical solution from the literature. Thereby, the effect of voltage on the mechanical load results could also be examined. The thicknesses of the FG substrate and PFRC actuator layers are taken as $h = 3 \times 10^{-3}$ m and $h_p = 250$ µm, respectively. PFRC

layer is made of PZT5H with the material properties defined in Table 1. Besides, the engineering constants at the bottom location ($x_3 = 0$) of the isotropic FG plate are regarded as: $E_0 = 200$ GPa and v = 0.3. The Poisson's ratio, v is assumed as constant over the FG plate and the Young's modulus, E is varied as an exponential function of the thickness coordinate as:

$$E = E_0 e^{\lambda x_3} \tag{34}$$

with a parameter λ characterizing the inhomogeneity of the FG material throughout the thickness that can be described as:

$$\lambda = \frac{\ln\left(\frac{E_h}{E_0}\right)}{h} \tag{35}$$

where E_h refers to the elasticity modulus of the FG plate at $x_3 = h$. The mechanical and electrical boundary conditions over the FG plate are as follows:

$$u_2(x_2, x_3) = u_3(x_2, x_3) = \phi_p(x_2, x_3) = 0$$
 at $x_1 = 0$ and $x_1 = a$ (36a)

$$u_1(x_1, x_3) = u_3(x_1, x_3) = \phi_p(x_1, x_3) = 0$$
 at $x_2 = 0$ and $x_2 = b$ (36b)

$$\phi_p(x_1, x_2, x_3) = 0$$
 at $0 \le x_3 \le h$ (36c)

Also, the imposed bisinusoidal mechanical and electrical loadings on top surface of the PFRC plate are defined as:

$$q(x_1, x_2, x_3 = h + h_p) = q_0 \sin\left(\frac{\pi x_1}{a}\right) \sin\left(\frac{\pi x_2}{h}\right)$$
 with $q_0 = -40 \text{ N/m}^2$ (37a)

$$\phi_p(x_1, x_2, x_3 = h + h_p) = V \sin\left(\frac{\pi x_1}{a}\right) \sin\left(\frac{\pi x_2}{h}\right) \qquad \text{with } V = 0 \pm 100 \tag{37b}$$

This configuration enables the study of the behavior of the functionally graded plate under both mechanical and various electrical potential loads applied to the PFRC layer, with an emphasis on displacement, and stress values. The results obtained were then compared to the analytical solution presented in the literature [16]. Utilizing simply-supported boundary conditions as well as with the zero electrical potential conditions at the edges of the PFRC layer make the four primary unknowns (u_1, u_2, u_3, ϕ_p) to be written in terms of a sinus and cosinus admissible functions that yields a set of homogenous algebraic equations to be solved [16]. To be more convenient, the displacement and stress values are normalized as follows:

$$\bar{u}_1 = \frac{E_0 h^2}{a_0 a^3} u_1 \qquad \bar{u}_3 = \frac{100 E_0 h^3}{a_0 a^4} u_3 \qquad \{\bar{\sigma}_1 \quad \bar{\sigma}_2 \quad \bar{\tau}_{12}\}^T = \frac{h^2}{a^2 a_0} \{\sigma_1 \quad \sigma_2 \quad \tau_{12}\}^T$$
(38)

The normalized in-plane and transverse displacements (\bar{u}_1, \bar{u}_3) , along with the in-plane normal and shear stresses $(\bar{\sigma}_1, \bar{\sigma}_2, \bar{\tau}_{12})$, for an FG substrate with $\frac{E_h}{E_0} = 10$ are provided in Tables 2 and 3, respectively. Thin plate (a/h = 100) is subjected to bisinusoidal distributed mechanical loading together with/without applied voltages.

Tables 2 and 3 indicate that the present results obtained from FGL-IGA are in good agreement with the exact solutions and the maximum deviation from the exact values for displacements do not exceed %1.06. It is also clear that applying a positive voltage (V = +100) to the PFRC layer causes the substrate to bend in the opposite direction of the mechanical load, thereby reducing the mechanical deformations. In contrast,

when the voltage polarity is negative (V = -100), the actuator bends the substrate in the direction of the mechanical load, which results in an increase in the mechanical deformations.

Table 2. Normalized displacement responses of the FG substrate plate $(E_h/E_o=10)$ for various applied voltages (V) to the top surface (a/h=100)

V	Theory	\bar{u}_3 $(x_1 = a/2, x_2 = b/2, x_3 = h/2)$	Error Percentage (%)	$\bar{u}_1(x_1 = 0, x_2 = b/2, x_3 = 0)$ $\bar{u}_1(x_1 = 0, x_2 = b/2, x_3 = h)$	Error Percentage (%)
0	Present	-0.9139	0.17	-0.0195 0.0093	0.00
	Exact [16]	-0.9155		-0.0195 0.0093	
100	Present	0.9296	0.77	-0.0201 -0.0494	0.50 0.60
	Exact [16]	0.9368		-0.0202 -0.0497	
-100	Present	-2.7534	0.52	-0.0190 0.0679	1.06 0.44
	Exact [16]	-2.7678		-0.0188 0.0682	

Table 3. Normalized stress responses of the FG substrate plate ($E_h/E_o=10$) for various applied voltages (V) to the top surface (a/h=100)

V	Theory		$\bar{\sigma}_2(x_1 = a/2, x_2 = b/2, x_3 = 0)$ $\bar{\sigma}_2(x_1 = a/2, x_2 = b/2, x_3 = h)$	
0	Present	0.0880	0.0879	-0.0473
		-0.4189	-0.4198	0.2257
	Exact [16]	0.0874	0.0873	-0.0470
		-0.4161	-0.4170	0.2243
100	Present	0.0288	-0.1148	0.0231
		1.6160	0.1778	-0.4803
	Exact [16]	0.0291	-0.1145	0.0230
		1.6124	0.1751	-0.4813
-100	Present	0.1472	0.2907	-0.1178
		-2.4539	-1.0174	0.9317
	P . (14)	0.1457	0.2892	-0.1171
	Exact [16]	-2.4446	-1.0090	0.9298

It is evident from Fig. 6 that the FGL-IGA stress results are virtually indistinguishable from the exact ones and the stress distribution across the thickness is nonlinear, resulting from the nonzero gradient of the Young's modulus defined in Eq. (34). Furthermore, the maximum stress observed at the interface between the substrate and the PFRC layer can be attributed to the Young's modulus reaching its highest value $(E_h/E_0 = 10)$ at this location.

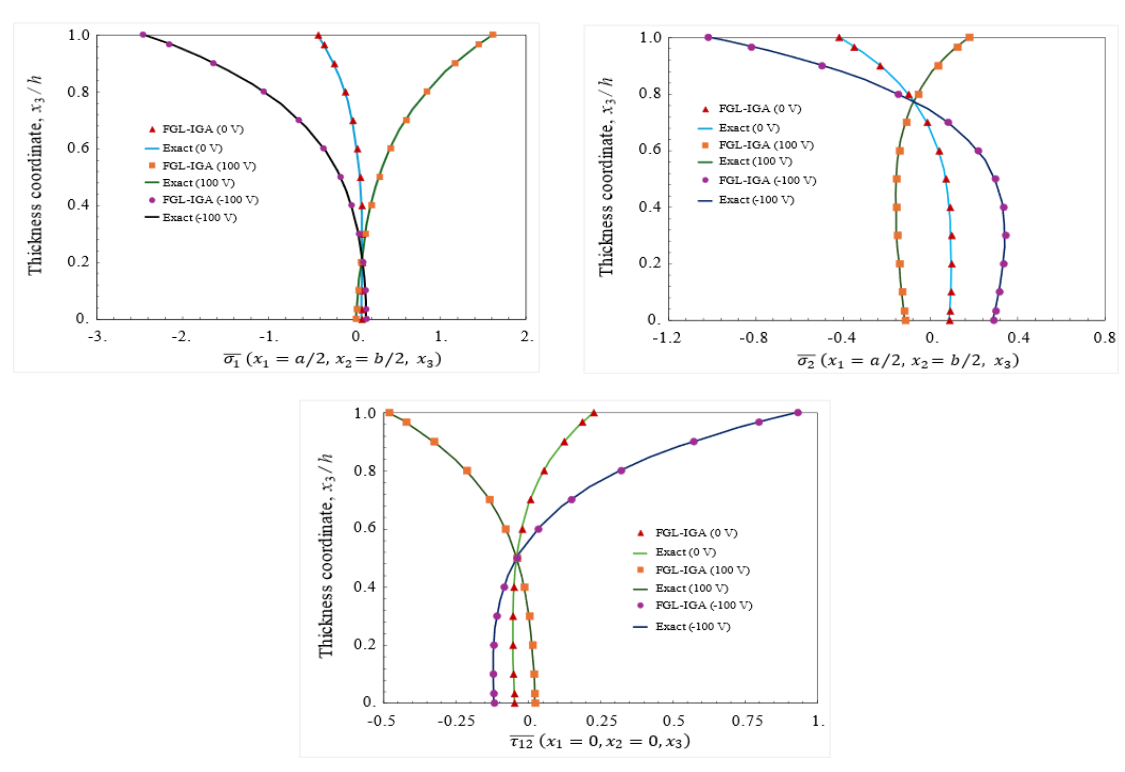


Fig. 6. Distributions of in-plane normal and shear stress throughout the thickness of thin (a/h = 100)FG plate $\left(\frac{E_h}{E_o} = 10\right)$ with/without applied voltages

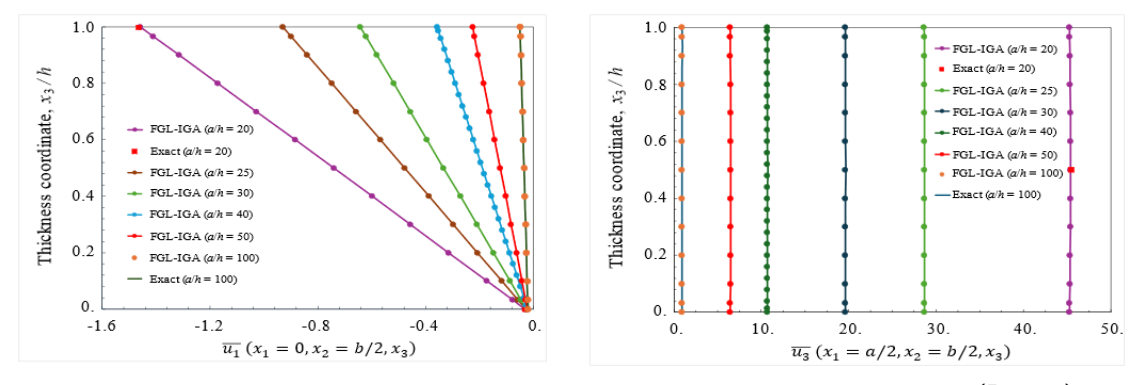


Fig. 7. Distributions of in-plane and transverse displacement throughout the thickness of FG plate $\left(\frac{E_h}{E_0} = 10\right)$ for various span/thickness ratios (V = 100)

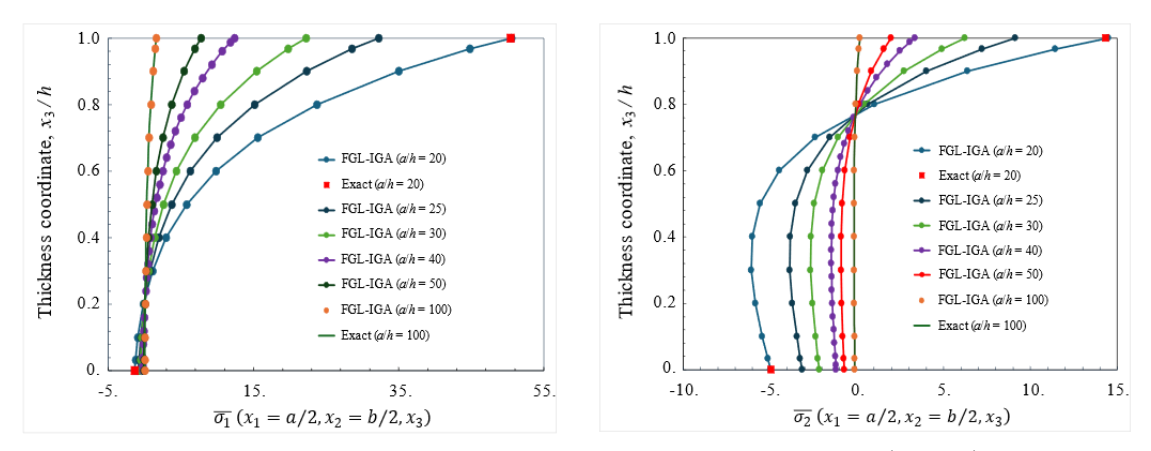


Fig. 8. Distributions of in-plane normal stresses throughout the thickness of FG plate $\left(\frac{E_h}{E_0} = 10\right)$ for various span/thickness ratios

Figs. 7 and 8 show how span/thickness ratio affects through-the-thickness displacement and stress variations for the range of moderately thick to thin plates under applied voltage (V = 100) and mechanical loadings given in Eqs. (37a-b). By keeping the thickness of the FG plate is fixed (h = 0.003 m) and modifying the in-plane dimensions, several static analyses have been conducted. Otherwise, altering the thickness would result in the inhomogeneity parameter λ to be modified in accordance with Eq. (35). It can be seen from Figs. 7 and 8 that the in-plane displacements behave linearly along the thickness direction, while the transverse displacements remain constant, and the normal stresses follow a nonlinear pattern. The results obtained are consistent with the exact solution [16], and increasing thickness leads to a significant rise in both displacements and stresses.

4. Conclusions

In this study, an isogeometric finite element has been developed to obtain the static response of functionally graded piezoelectric plates. Thanks to its ability to allow the exponential variation of both piezoelectric and mechanical properties along the thickness, the formulation can be applied to any plate system, whether it is created by grading solely the piezoelectric material or by varying the properties of isotropic or orthotropic materials and placing a homogeneous piezoelectric actuator on top. To validate the present formulation, the results obtained from FGL-IGA have been compared with those reported in literature and the results show that FGL-IGA is in excellent agreement with the exact ones. Also, the FGL-IGA displacement and stress results in overlapping with the analytical ones for a wide range of span/thickness ratio, i.e., a/h = 20 to a/h = 100 (from moderately thick to thin plates).

This study serves as an initial attempt to showcase the efficiency of isogeometric layerwise analysis for functionally graded piezoelectric plates. It can be further extended to static or transient analyses of more complex geometries, such as those with curved boundaries or internal holes within the FG piezoelectric plate domain, in future work.

Conflict of interests

The author(s) declared no potential conflicts of interest with respect to the research, authorship, and/or publication of this article.

Funding

This research received no external funding.

Data availability statement

Data generated during the current study are available from the corresponding author upon reasonable request.

Appendix A

The global stiffness coefficients defined in Eq. (3) can be obtained in terms of local stiffness values and angle, $\theta^{(k)}$ as:

$$\bar{Q}_{11}^{(k)} = Q_{11}^{(k)} \cos^4 \theta^{(k)} + 2 \left(Q_{12}^{(k)} + 2 Q_{66}^{(k)} \right) \sin^2 \theta^{(k)} \cos^2 \theta^{(k)} + Q_{22}^{(k)} \sin^4 \theta^{(k)} \tag{A1a}$$

$$\bar{Q}_{12}^{(k)} = \left(Q_{11}^{(k)} + Q_{22}^{(k)} - 4Q_{66}^{(k)}\right) \sin^2\theta^{(k)} \cos^2\theta^{(k)} + Q_{12}^{(k)} \left(\sin^4\theta^{(k)} + \cos^4\theta^{(k)}\right) \tag{A1b}$$

$$\bar{Q}_{22}^{(k)} = Q_{11}^{(k)} \sin^4 \theta^{(k)} + 2(Q_{12}^{(k)} + 2Q_{66}^{(k)}) \sin^2 \theta^{(k)} \cos^2 \theta^{(k)} + Q_{22}^{(k)} \cos^4 \theta^{(k)}$$
 (A1c)

$$\bar{Q}_{16}^{(k)} = \left(Q_{11}^{(k)} - Q_{12}^{(k)} - 2Q_{66}^{(k)}\right)\sin\theta^{(k)}\cos^3\theta^{(k)} + \left(Q_{12}^{(k)} - Q_{22}^{(k)} + 2Q_{66}^{(k)}\right)\sin^3\theta^{(k)}\cos\theta^{(k)} \tag{A1d}$$

$$\bar{Q}_{26}^{(k)} = \left(Q_{11}^{(k)} - Q_{12}^{(k)} - 2Q_{66}^{(k)}\right) \sin^3\theta^{(k)} \cos\theta^{(k)} + \left(Q_{12}^{(k)} - Q_{22}^{(k)} + 2Q_{66}^{(k)}\right) \sin\theta^{(k)} \cos^3\theta^{(k)} \tag{A1e}$$

$$\bar{Q}_{66}^{(k)} = \left(Q_{11}^{(k)} + Q_{22}^{(k)} - 2Q_{12}^{(k)} - 2Q_{66}^{(k)}\right) \sin^2\theta^{(k)} \cos^2\theta^{(k)} + Q_{66}^{(k)} \left(\sin^4\theta^{(k)} + \cos^4\theta^{(k)}\right) \tag{A1f}$$

$$\bar{Q}_{44}^{(k)} = Q_{44}^{(k)} \cos^2 \theta^{(k)} + Q_{55}^{(k)} \sin^2 \theta^{(k)} \tag{A1h}$$

$$\bar{Q}_{45}^{(k)} = (Q_{44}^{(k)} - Q_{55}^{(k)})\cos\theta^{(k)}\sin\theta^{(k)} \tag{A1i}$$

$$\bar{Q}_{EE}^{(k)} = Q_{EE}^{(k)} \cos^2 \theta^{(k)} + Q_{AA}^{(k)} \sin^2 \theta^{(k)}$$
(A1j)

Appendix B

$$\boldsymbol{B}_{\boldsymbol{u}} = \begin{bmatrix} \boldsymbol{B}_{\boldsymbol{u}}^1 & \boldsymbol{B}_{\boldsymbol{u}}^2 & \cdots & \boldsymbol{B}_{\boldsymbol{u}}^j & \cdots & \boldsymbol{B}_{\boldsymbol{u}}^{nenz} \end{bmatrix}$$
(B1a)

$$\boldsymbol{B}_{\boldsymbol{u}}^{j} = \begin{bmatrix} \frac{\partial R_{1}}{\partial x_{1}} \bar{R}_{j} & 0 & 0 & \frac{\partial R_{2}}{\partial x_{1}} \bar{R}_{j}(\zeta) & 0 & 0 & \cdots & \frac{\partial R_{nen}}{\partial x_{1}} \bar{R}_{j} & 0 & 0 \\ 0 & \frac{\partial R_{1}}{\partial x_{2}} \bar{R}_{j} & 0 & 0 & \frac{\partial R_{2}}{\partial x_{2}} \bar{R}_{j} & 0 & \cdots & 0 & \frac{\partial R_{nen}}{\partial x_{2}} \bar{R}_{j} & 0 \\ 0 & 0 & R_{1} \frac{\partial \bar{R}_{j}}{\partial x_{3}} & 0 & 0 & R_{2} \frac{\partial \bar{R}_{j}}{\partial x_{3}} & \cdots & 0 & 0 & R_{nen} \frac{\partial \bar{R}_{j}}{\partial x_{3}} \\ R_{1} \frac{\partial \bar{R}_{j}}{\partial x_{3}} & 0 & \frac{\partial R_{1}}{\partial x_{1}} \bar{R}_{j} & R_{2} \frac{\partial \bar{R}_{j}}{\partial x_{3}} & 0 & \frac{\partial R_{2}}{\partial x_{3}} \bar{R}_{j} & \cdots & R_{nen} \frac{\partial \bar{R}_{j}}{\partial x_{3}} & 0 & \frac{\partial R_{nen}}{\partial x_{1}} \bar{R}_{j} \\ 0 & R_{1} \frac{\partial \bar{R}_{j}}{\partial x_{3}} & \frac{\partial R_{1}}{\partial x_{2}} \bar{R}_{j} & 0 & R_{2} \frac{\partial \bar{R}_{j}}{\partial x_{3}} & \frac{\partial R_{2}}{\partial x_{2}} \bar{R}_{j} & \cdots & 0 & R_{nen} \frac{\partial \bar{R}_{j}}{\partial x_{3}} & \frac{\partial R_{nen}}{\partial x_{2}} \bar{R}_{j} \\ \frac{\partial R_{1}}{\partial x_{2}} \bar{R}_{j} & \frac{\partial R_{1}}{\partial x_{1}} \bar{R}_{j} & 0 & \frac{\partial R_{2}}{\partial x_{2}} \bar{R}_{j} & 0 & \cdots & \frac{\partial R_{nen}}{\partial x_{2}} \bar{R}_{j} & \frac{\partial R_{nen}}{\partial x_{1}} \bar{R}_{j} & 0 \end{bmatrix}$$
(B1b)

$$\boldsymbol{B}_{\boldsymbol{\Phi}} = \begin{bmatrix} \boldsymbol{B}_{\boldsymbol{\Phi}}^1 & \boldsymbol{B}_{\boldsymbol{\Phi}}^2 & \cdots & \boldsymbol{B}_{\boldsymbol{\Phi}}^j & \cdots & \boldsymbol{B}_{\boldsymbol{\Phi}}^{nenz} \end{bmatrix}$$
(B2a)

$$\boldsymbol{B}_{\boldsymbol{\Phi}}^{j} = \begin{bmatrix} -\frac{\partial R_{1}}{\partial x_{1}} \bar{R}_{j} & -\frac{\partial R_{2}}{\partial x_{1}} \bar{R}_{j} & \cdots & -\frac{\partial R_{nen}}{\partial x_{1}} \bar{R}_{j} \\ -\frac{\partial R_{1}}{\partial x_{2}} \bar{R}_{j} & -\frac{\partial R_{2}}{\partial x_{2}} \bar{R}_{j} & \cdots & -\frac{\partial R_{nen}}{\partial x_{2}} \bar{R}_{j} \\ -R_{1} \frac{\partial \bar{R}_{j}}{\partial x_{3}} & -R_{2} \frac{\partial \bar{R}_{j}}{\partial x_{3}} & \cdots & -R_{nen} \frac{\partial \bar{R}_{j}}{\partial x_{3}} \end{bmatrix}$$
(B2b)

References

- [1] Koizumi M (1993) The concept of FGM. Ceram Trans Funct Grad Mater 3–10.
- [2] Yamanouchi M, Koizumi M, Hirai T, Shiota I (1990) Proceedings of the First International Symposium of Functionally Graded Materials
- [3] Mori T, Tanaka K (1973) Average stress in matrix and average elastic energy of materials with misfitting inclusions. Acta Metall 21:571–4. https://doi.org/10.1016/0001-6160(73)90064-3
- [4] Koizumi M (1997) FGM activities in Japan. Compos Part B 28:1–4. https://doi.org/10.1016/S1359-8368(96)00016-9
- [5] Reddy JN (2000) Analysis of functionally graded plates. Int J Numer Methods Eng 47:663–84. https://doi.org/10.1002/(SICI)1097-0207(20000110/30)47:1/3<663::AID-NME787>3.0.CO;2-8
- [6] Cheng ZQ, Batra RC (2000) Three-dimensional thermoelastic deformations of a functionally graded elliptic plate. Compos Part B Eng 31:97–106. https://doi.org/10.1016/S1359-8368(99)00069-4
- [7] Carrera E, Brischetto S, Cinefra M, Soave M (2011) Effects of thickness stretching in functionally graded plates and shells. Compos Part B Eng 42:123–33. https://doi.org/10.1016/j.compositesb.2010.10.005
- [8] Carrera E, Cinefra M, Zappino E, Petrolo M (2014) Finite Element Analysis of Structures Through Unified Formulation. Wiley. https://doi.org/10.1002/9781118536643
- [9] Carrera E, Brischetto S, Robaldo A (2008) Variable kinematic model for the analysis of functionally graded material plates. AIAA J 46:194–203. https://doi.org/10.2514/1.32490
- [10] Brischetto S, Carrera E (2010) Advanced mixed theories for bending analysis of functionally graded plates. Comput Struct 88:1474–83. https://doi.org/10.1016/j.compstruc.2008.04.004
- [11] Brischetto S (2009) Classical and mixed advanced models for sandwich plates embedding functionally graded cores. J Mech Mater Struct 4:13–33. https://doi.org/10.2140/jomms.2009.4.13
- [12] Chopra I (2002) Review of State of Art of Smart Structures. AIAA J 40:16–9.
- [13] Zhu X, Meng Z (1995) Operational principle, fabrication and displacement characteristics of a functionally gradient piezoelectric ceramic actuator. Sensors Actuators A 48:169–76. https://doi.org/10.1016/0924-4247(95)00996-5
- [14] Mallik N, Ray MC (2003) Effective Coefficients of Piezoelectric Fiber-Reinforced Composites. AIAA J 41:704– 10. https://doi.org/10.2514/2.2001
- [15] Ray MC, Sachade HM (2006) Finite element analysis of smart functionally graded plates. Int J Solids Struct 43:5468–84. https://doi.org/10.1016/j.ijsolstr.2005.06.096
- [16] Ray MC, Sachade HM (2006) Exact solutions for the functionally graded plates integrated with a layer of piezoelectric fiber-reinforced composite. J Appl Mech Trans ASME 73:622–32. https://doi.org/10.1115/1.2165230
- [17] Zhong Z, Shang ET (2003) Three-dimensional exact analysis of a simply supported functionally gradient piezoelectric plate. Int J Solids Struct 40:5335–52. https://doi.org/10.1016/S0020-7683(03)00288-9
- [18] Zenkour AM, Alghanmi RA (2021) Hygro-thermo-electro-mechanical bending analysis of sandwich plates with FG core and piezoelectric faces. Mech Adv Mater Struct 28:282–94. https://doi.org/10.1080/15376494.2018.1562134
- [19] Rouzegar J, Abbasi A (2017) A refined finite element method for bending of smart functionally graded plates. Thin-Walled Struct 120:386–96. https://doi.org/10.1016/j.tws.2017.09.018

- [20] Shiyekar SM, Kant T (2011) Higher order shear deformation effects on analysis of laminates with piezoelectric fibre reinforced composite actuators. Compos Struct 93:3252–61. https://doi.org/10.1016/j.compstruct.2011.05.016
- [21] Chanda A, Sahoo R (2020) Flexural Behavior of Functionally Graded Plates with Piezoelectric Materials. Arab J Sci Eng 45:9227–48. https://doi.org/10.1007/s13369-020-04699-w
- [22] Dung NT, Minh P Van, Hung HM, Tien DM (2021) The Third-Order Shear Deformation Theory for Modeling the Static Bending and Dynamic Responses of Piezoelectric Bidirectional Functionally Graded Plates. Adv Mater Sci Eng. https://doi.org/10.1155/2021/5520240
- [23] Cottrell JA, Hughes TJR, Bazilevs Y (2009) Isogeometric Analysis Toward Integration of CAD and FEA. United Kingdom: John Wiley & Sons Ltd.
- [24] Hughes TJR, Cottrell JA, Bazilevs Y (2005) Isogeometric analysis: CAD, finite elements, NURBS, exact geometry and mesh refinement. Comput Methods Appl Mech Eng 194:4135–95. https://doi.org/10.1016/j.cma.2004.10.008
- [25] Nguyen VP, Anitescu C, Bordas SPA, Rabczuk T (2015) Isogeometric analysis: An overview and computer implementation aspects. Math Comput Simul 117:89–116. https://doi.org/10.1016/j.matcom.2015.05.008
- [26] Thai CH, Kulasegaram S, Tran L V, Nguyen-Xuan H (2014) Generalized shear deformation theory for functionally graded isotropic and sandwich plates based on isogeometric approach. Comput Struct 141:94–112. https://doi.org/https://doi.org/10.1016/j.compstruc.2014.04.003
- [27] Nguyen TN, Thai CH, Luu AT, Nguyen-Xuan H, Lee J, Kulasegaram S, et al. (2019) NURBS-based postbuckling analysis of functionally graded carbon nanotube-reinforced composite shells. Comput Methods Appl Mech Eng 347:983–1003. https://doi.org/10.1016/j.cma.2019.01.011
- [28] Liu T, Li C, Wang C, Lai JW, Cheong KH (2020) A simple-fsdt-based isogeometric method for piezoelectric functionally graded plates. Mathematics 8:1–24. https://doi.org/10.3390/math8122177
- [29] Chen M, Chen H, Ma X, Jin G, Ye T, Zhang Y, et al. (2018) The isogeometric free vibration and transient response of functionally graded piezoelectric curved beam with elastic restraints. Results Phys 11:712–25. https://doi.org/10.1016/j.rinp.2018.10.019
- [30] Shi P (2022) Three-dimensional isogeometric analysis of functionally graded carbon nanotube-reinforced composite plates. Arch Appl Mech 92:3033–63. https://doi.org/10.1007/s00419-022-02224-z
- [31] Nguyen-Thoi T, Ly DK, Kattimani S, Thongchom C (2024) An electromechanical coupling isogeometric approach using zig-zag function for modeling and smart damping control of multilayer PFG-GPRC plates. Acta Mech 235:941–70. https://doi.org/10.1007/s00707-023-03785-y
- [32] Qian LF, Batra RC, Chen LM (2004) Static and dynamic deformations of thick functionally graded elastic plates by using higher-order shear and normal deformable plate theory and meshless local Petrov–Galerkin method. Compos Part B Eng 35:685–97. https://doi.org/10.1016/j.compositesb.2004.02.004
- [33] Shakeri M, Mirzaeifar R (2009) Static and dynamic analysis of thick functionally graded plates with piezoelectric layers using layerwise finite element model. Mech Adv Mater Struct 16:561–75. https://doi.org/10.1080/15376490802625514
- [34] Moleiro F, Mota Soares CM, Mota Soares CA, Reddy JN (2012) Assessment of a layerwise mixed least-squares model for analysis of multilayered piezoelectric composite plates. Comput Struct 108–109:14–30. https://doi.org/10.1016/j.compstruc.2012.04.002
- [35] Hasim KA, Kefal A (2022) A novel isogeometric layerwise element for piezoelectric analysis of laminated plates with straight/curvilinear fibers. Comput Methods Appl Mech Eng 399:115440. https://doi.org/10.1016/j.cma.2022.115440
- [36] Li G, Carrera E, Hou Y, Kulikov GM (2021) Multi-layered plate finite element models with node-dependent kinematics for smart structures with piezoelectric components. Chinese J Aeronaut 34:164–75. https://doi.org/10.1016/j.cja.2021.01.005
- [37] Piegl L, Tiller W (1997) The NURBS Book.
- [38] McNeel R (2010) Rhinoceros 3D.
- [39] Reddy JN (2003) Mechanics of Laminated Composite Plates and Shells Theory and Analysis 840.
- [40] Chandrupatla T, Belegundu A (2021) Introduction to Finite Elements in Engineering. 5th Edition. Cambridge University Press, Cambridge. https://doi.org/DOI:10.1017/9781108882293
- [41] Bathe KJ (1996) Finite Element Procedures. Englewood Cliffs: Prentice-Hall.